

HELIUM REIONIZATION SIMULATIONS. III. THE HELIUM LYMAN- α FOREST

PAUL LA PLANTE^{1,2}, HY TRAC², RUPERT CROFT², AND RENYUE CEN³

¹Center for Particle Cosmology, Department of Physics and Astronomy, University of Pennsylvania, Philadelphia, PA 19104, USA, plaplant@sas.upenn.edu

²McWilliams Center for Cosmology, Department of Physics, Carnegie Mellon University, Pittsburgh, PA 15213, USA

³Department of Astrophysical Science, Princeton University, Princeton NJ 08544, USA

ABSTRACT

In La Plante et al. (2017), we presented a new suite of hydrodynamic simulations with the aim of accurately capturing the process of helium II reionization. In this paper, we discuss the observational signatures present in the He II Ly α forest. We show that the effective optical depth of the volume τ_{eff} is not sufficient for capturing the ionization state of helium II, due to the large variance inherent in sightlines. However, the He II flux PDF can be used to determine the timing of helium II reionization. The amplitude of the one-dimensional flux power spectrum can also determine the ionization state of helium II. We show that even given the currently limited number of observations (~ 50 sightlines), measurements of the flux PDF can yield information about helium II reionization. Further, measurements using the one-dimensional power spectrum can provide clear indications of the timing of reionization, as well as the relative bias of sources of ionizing radiation.

Keywords: cosmology: theory — intergalactic medium — large-scale structure of the universe — methods: numerical — quasars: general

1. INTRODUCTION

There has been much interest in understanding the reionization of helium II, using semi-analytic methods (Gleser et al. 2005; Furlanetto & Oh 2008b,a, 2009; Dixon et al. 2014), numerical simulations (Croft et al. 1997; McQuinn et al. 2009, 2011; Compostella et al. 2013, 2014; Puchwein et al. 2015; Bolton et al. 2016), and observations (Jakobsen et al. 1994; Reimers et al. 1997; Zheng et al. 2008; Dixon & Furlanetto 2009; Syphers & Shull 2014; Worseck et al. 2014). Helium II reionization is thought to be driven by highly energetic photons emitted by quasars. Due to photoheating of gas in the intergalactic medium (IGM) from these high-energy photons, helium II reionization leaves an important signature on the thermal state of the IGM. Knowledge of the thermal state is important for making measurements of quantities related to the Ly α forest, such as the free-streaming length of warm dark matter (Viel et al. 2005; Iršič et al. 2017). However, such temperature measurements are difficult to make and have large systematic or statistical uncertainties (Schaye et al. 1999; McDonald et al. 2001; Becker et al. 2011; Boera et al. 2014). Further, these methods rely on correctly calibrating the state of the hydrogen Ly α forest with the gas temperature, which is fraught with difficulty.

A more appealing approach is to measure the ionization state of helium directly, without relying on calibra-

tion. Just as the Ly α transition for neutral hydrogen (H I) appears as absorption features in spectra of radiation from distant quasars, so too does the transition for singly ionized helium (He II) appear. This feature appears at 304 Å in the rest-frame of the absorbing gas, a shift of a factor of four in frequency space compared to the hydrogen transition due to the additional proton in the helium nucleus. As with the H I Ly α forest, the very high transition strength means a very small amount of singly ionized helium can lead to total absorption of the incoming radiation. Typically, neutral fractions of $f_{\text{HeII}} \gtrsim 10^{-3}$ can produce a Gunn-Peterson trough (Gunn & Peterson 1965), making detection of the early stages of helium II reionization difficult. Despite this difficulty, measuring the ionization status of helium from the He II Ly α forest provides a more direct probe than using temperature measurements or the H I Ly α forest.

Part of the difficulty in observing the He II Ly α forest lies in contamination of high-density systems at lower redshift. Lyman-limit systems (LLSs) and damped Ly α systems (DLAs) which are at intermediate redshift (say at z_{LLS}) between the comparatively high-redshift IGM gas we are interested in observing (say at z_{IGM}) and observers on Earth can absorb much of the radiation above the ionization potential of hydrogen at 912 Å. Quantitatively, if $912(1 + z_{\text{LLS}}) \gtrsim 304(1 + z_{\text{IGM}})$, then the lower-

redshift LLS or DLA will obfuscate the He II Ly α forest of interest. Due to the relative abundance of LLSs and DLAs at low redshift, only a small number of quasar sightlines are suitable for measuring the He II Ly α forest (Møller & Jakobsen 1990; Zheng et al. 2005). Indeed, despite having more than 150,000 quasar sightlines from BOSS alone (Dawson et al. 2013), to date there have been only about 50 sightlines for which the He II Ly α forest has been measured (Syphers et al. 2009b,a, 2012).¹ These measurements have provided significant insight to the general picture of helium II reionization: at redshifts $z > 3$, a Gunn-Peterson trough has been detected (Jakobsen et al. 1994; Zheng et al. 2008; Syphers & Shull 2014); below this redshift, helium II reionization becomes patchy, showing extended regions of absorption and transmission corresponding to the ionization level of the gas (Reimers et al. 1997); finally, by redshift $z \sim 2.7$, helium appears to be totally reionized (Dixon & Furlanetto 2009; Worseck et al. 2011). However, information beyond this general picture is difficult to glean from the current limited set of He II spectra. To this end, measurements providing additional information about helium II reionization is an important application of current and ongoing research.

In La Plante & Trac (2016) (hereafter Paper I) of this paper series, we provided a method by which simulation volumes can be populated with quasars in order to reproduce the quasar luminosity function (QLF) at various redshift epochs (Masters et al. 2012; Ross et al. 2013; McGreer et al. 2013) as well as quasar clustering (White et al. 2012). In La Plante et al. (2017) (hereafter Paper II), we presented a new suite of large-scale simulations with the purpose of exploring helium II reionization. These simulations include N -body, hydrodynamics, and radiative transfer solved simultaneously, which allows us to capture the evolution of the IGM with newfound accuracy. Based on the output of these simulations, we are able to generate synthetic Ly α sightlines for H I and He II. In this paper, we present specific results about the He II spectra, and discuss ways to learn about the timing of helium II reionization.

We organize the rest of this paper as follows. In Section 2, we briefly discuss our suite of simulations. In Section 3, we discuss the He II Ly α forest, and various measurements that can be made using the spectra. In Section 4, we discuss prospects for detecting helium II reionization properties given the current measurements. In Section 5, we summarize our findings.

¹ It should be noted, though, that a single sightline of, *e.g.*, 100 physical Mpc, can yield multiple measurements of a given statistic by dividing the total sightline into multiple smaller segments of moderate size (*e.g.*, 10 physical Mpc as in Worseck et al. 2014).

Throughout this work, we assume a Λ CDM cosmology with $\Omega_m = 0.27$, $\Omega_\Lambda = 0.73$, $\Omega_b = 0.045$, $h = 0.7$, $\sigma_8 = 0.8$, and $Y_{\text{He}} = 0.24$. These values are consistent with the *WMAP*-9 year results (Hinshaw et al. 2013).

2. RADIATION-HYDRODYNAMIC SIMULATIONS

In Paper II, we presented a new suite of hydrodynamic simulations with radiative transfer, conducted with the goal of studying helium II reionization. Here, we summarize the properties of the simulations that are relevant to this paper’s results. Radiation-hydrodynamic simulations are run with the RadHydro code, which combines N -body and hydrodynamic algorithms (Trac & Pen 2004) with an adaptive ray-tracing algorithm (Trac & Cen 2007) to directly and simultaneously solve collisionless dark matter, collisional gas dynamics, and radiative transfer of ionizing photons. The simulations in Paper II employ 2048^3 dark matter particles, and 2048^3 hydrodynamic resolution elements in a fixed-grid Eulerian scheme. The grid for radiative transfer contains 512^3 resolution elements. The simulation code has already been used to study hydrogen reionization (Trac & Cen 2007; Trac et al. 2008; Battaglia et al. 2013). For additional details about the simulations, see Paper II.

The simulations contain two features in particular that bear mentioning. First, the simulations include a patchy model for hydrogen reionization developed in Battaglia et al. (2013). The midpoint of reionization has been set such that $\bar{z}_{\text{re}} = 8$, but in general, regions of high-density undergo reionization before regions of low density. By incorporating an “inside-out” reionization scenario, we ensure that the thermal state of the IGM before helium II reionization accurately reflects the impact of hydrogen reionization. Second, the contribution of galaxies to the UV background Γ_{gal} is modified on-the-fly in order to reproduce the observed effective optical depth τ_{eff} of the H I Ly α forest. The quantity τ_{eff} is related to the flux of the Ly α forest F , defined for every location in the volume as $F \equiv e^{-\tau}$. In this expression, τ is the optical depth of Ly α radiation. Note that $\bar{F} \neq e^{-\bar{\tau}}$. Values of $F \sim 0$ represent total absorption (typically the result of a high density of neutral hydrogen), and values of $F \sim 1$ represent total transmission. It is then possible to define the effective optical depth of the entire volume, namely as:

$$\langle F \rangle_{\text{HI}} = e^{-\tau_{\text{eff,HI}}}, \quad (1)$$

where $\langle F \rangle_{\text{HI}}$ is the average flux of the H I Ly α forest of the volume, with an analogous definition for He II. Specifically, we match τ_{eff} as parameterized in Lee et al. (2015). These results are based primarily on data from the seventh data release of the Sloan Digital Sky survey (SDSS DR7) presented in Becker et al. (2013). Modifying Γ_{gal} while the simulations are running means we

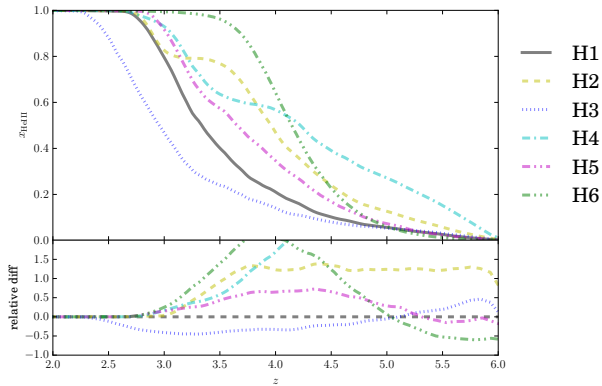


Figure 1. The ionization level of simulations as a function of redshift for the simulation suite presented in Paper II. Simulation H1 is the fiducial reionization scenario. Simulations H2 and H3 increase and decrease the amplitude of the QLF, respectively, by a factor of two. Simulation H4 uses the same sources as H1, but increases the photon production per quasar by a factor of two. Simulation H5 uses a slightly different QLF from the other simulations. Simulation H6 uses a uniform UV-background instead of explicit quasar sources. The models are discussed further in Section 2.

do not need to renormalize the Ly α forest in post-processing, as previous studies of the Ly α forest have done (*e.g.*, Bolton et al. 2009). This feature allows us to more easily compare the results between simulations and observations.

As explained in detail in Paper I, the simulation volumes are populated with quasars such that the observed QLF is matched between redshifts $2 \leq z \leq 6$ (Masters et al. 2012; Ross et al. 2013; McGreer et al. 2013), as well as the clustering measurements at $z \sim 2.4$ (White et al. 2012). For individual quasar objects, we use the SED from Lusso et al. (2015), which has a spectral index of $\alpha = 1.7$ ($f_\nu \propto \nu^{-\alpha}$) for $\lambda \leq 912 \text{ \AA}$, and a spectral index of $\alpha = 0.61$ for $\lambda > 912 \text{ \AA}$.

In Paper II, we presented a suite of six simulations, with different quasar properties. We will now briefly summarize each of these simulations. Simulation H1 is the fiducial reionization model, which uses the QLF combining the various measurements at distinct redshift epochs and the SED of Lusso et al. (2015). Simulation H2 increases the amplitude of the QLF by a factor of 2, leading to an earlier reionization scenario. Simulation H3 decreases the amplitude of the QLF by a factor of 2, leading to a late reionization time. Simulation H4 increases the normalization of the SED by a factor of 2, so that a given quasar with a given magnitude M will have a luminosity at 912 \AA L_{912} that is two times greater as that provided by the SED of Lusso et al. (2015). Simulation H5 uses a slightly different method for combining the QLF from distinct redshift epochs than Simulation H1, but uses the same SED. Simulation H6 does not have explicit quasar sources, but instead uses a uniform UV background with the

photoionization and photoheating rates as specified by Haardt & Madau (2012). Rather than simply using the rates “as is,” we scale them to match the observed value of $\tau_{\text{eff,HI}}$, as with the other simulations. See Paper II for further details about each of the simulations. Figure 1 shows the ionization fraction of the various simulations as a function of redshift.

3. HE II LY α FOREST MEASUREMENTS

At each time step in the simulation, we generate synthetic Ly α sightlines on-the-fly for H I and He II. The measurements of $\tau_{\text{eff,HI}}$ for the H I sightlines allow for modifying Γ_{gal} to ensure that the value is matched at all times in the simulation. Determining He II from the synthetic sightlines allows for a more straightforward connection with the ionization state of helium in the volume. We will now turn to specific observables related to the He II Ly α forest.

3.1. Effective Optical Depth

The effective optical depth τ_{eff} , as noted in Eqn. (1), is defined in terms of the average flux in the volume. As with the H I Ly α transition, the strength of the He II transition ensures that only a very small amount of singly-ionized helium is necessary to completely absorb incoming radiation. As a result, measurement of $\tau_{\text{eff,HeII}}$ is most sensitive to the end of reionization. Further, due to the very large comoving size of He III regions (typically tens of Mpc in diameter), there is a large variation between different sightlines in the simulation volume, or even along a given sightline. One significant reason for this is that the correlation length s_0 of quasars, defined by the three-dimensional two-point correlation function $\xi(s) = (s/s_0)^{-2}$ (*e.g.*, White et al. 2012), is comparable to, but slightly larger than, the mean free path of $h\nu = 54.4 \text{ eV}$ photons for $f_{\text{HeIII}} \sim 0.8$ at $z \sim 3$. Accordingly, until there is overlap of ionized regions, there are large contiguous regions of He II and He III. Ultimately, this results in large variation along a line of sight. Furthermore, these ionization regions typically do not overlap until the tail-end of reionization. This variation is especially prevalent while helium II reionization is proceeding. In other words, due to the large coherence of the doubly ionized regions, the observed optical depth can vary greatly from sightline to sightline, and so there should be a large variance in the measurements. This variation is in addition to any inherent variance in $\tau_{\text{eff,HeII}}$, primarily due to density fluctuations.

Figure 2 shows $\tau_{\text{eff,HeII}}$ as a function of redshift averaged over the whole simulation volume. The Figure also includes observational data from Worseck et al. (2014). These quasar spectra were taken using the cosmic origins spectrograph (COS) on the Hubble Space Telescope (HST). These spectra measure $\tau_{\text{eff,HeII}}$ for seg-

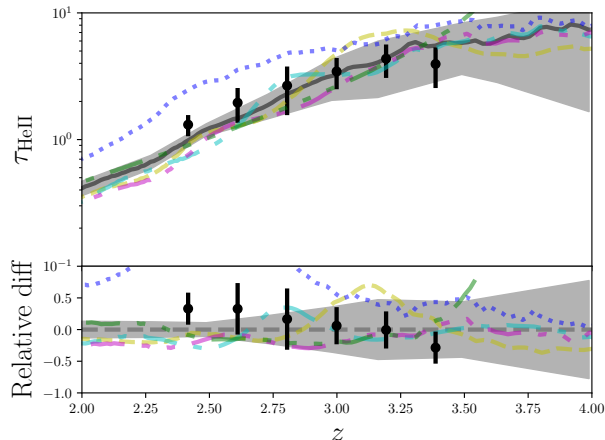


Figure 2. The effective optical depth of singly ionized helium $\tau_{\text{eff,HeII}}$ as a function of redshift for the suite of simulations. The black dots represent the binned observational data from [Worseck et al. \(2014\)](#), which are taken from HST/COS data. Color and line styles for the simulations are the same as in [Figure 1](#). The top panel shows the results for the simulations presented in [Paper II](#), and the bottom panel shows the relative difference to the fiducial simulation. As can be seen, there is a large degree of scatter in the measurements. By extension, none of the simulations is clearly disfavored. See [Section 3.1](#) for additional discussion.

ments of about 10 proper Mpc. The large sightline-to-sightline variation is evident in the observational data, which show very different values of $\tau_{\text{eff,HeII}}$ at the same redshift. The results from most of the simulations are largely consistent with the data at the redshifts for which data is available ($2.5 \lesssim z \lesssim 3.5$). The main exception to this is Simulation H3, which completes reionization at a significantly later time than the other simulations. Quantitatively, the redshift when the volume of Simulation H3 reaches an ionization fraction $x_{\text{HeIII}} \equiv n_{\text{HeIII}}/n_{\text{He}}$ of 99% is $z_{99} \sim 2.23$, compared to the timing of reionization in the fiducial scenario of $z_{99} \sim 2.69$. Given that this simulation completes reionization significantly later than the other ones, it is not surprising that the value of $\tau_{\text{eff,HeII}}$ in Simulation H3 is significantly higher than that of the other ones.

The gray shaded regions in [Figure 2](#) show the 1σ standard deviation estimated by calculating the standard deviation of flux $\sigma_F = \langle F^2 \rangle - \langle F \rangle^2$ computed using all sightlines in the volume. This standard deviation σ_F is then converted into the standard deviation of optical depth σ_τ using standard error propagation methods. Note that these methods implicitly assume that the distribution is Gaussian. The values in flux are generally not Gaussian, with most of the values tending to be either 0 or 1 (see [Figure 3](#)). Thus, the shaded regions of the plot are overly optimistic, and do not capture the true variance of $\tau_{\text{eff,HeII}}$ that is present in the volume. In particular, the shaded regions should extend to much higher values of $\tau_{\text{eff,HeII}}$, since these represent sightlines

with $\langle F \rangle \sim 0$.

An alternative to using error propagation is to use a different statistic for capturing the distribution of τ_{HeII} , or to use different sampling methods. For instance, instead of the mean and standard deviation, one could calculate $\langle F \rangle = \tau_{\text{eff,HeII}}$ for each sightline, and then calculate the median and central $\sim 68\%$ of central values (corresponding to 1σ). On the other hand, this approach poses problems related to the large difference of the median and the mean of the distribution of $\tau_{\text{eff,HeII}}$. In particular, at moderate redshift ($z \gtrsim 3$), the median of $\tau_{\text{eff,HeII}}$ measured per-sightline is significantly larger than the mean. As discussed above, for ionization fractions $x_{\text{HeIII}} \lesssim 99\%$, most sightlines demonstrate very high absorption, and so $\langle F \rangle \approx 0$. Though these high-absorption sightlines do not significantly alter $\langle F \rangle$ when computed for the entire volume, they represent a significant number of individual sightlines, making the median noticeably distinct from the mean.

Another possible way to circumvent the difficulties associated with error propagation is to use bootstrap resampling to provide an estimate on the distribution of the mean. The relevant parameter then becomes how many samples to use when estimating the variation on the mean. As noted in [Section 1](#), to date there have been roughly 50 He II sightlines observed. Naïvely, one might assume that using 50 sightlines in the bootstrap calculation would be a way to determine the variance of $\tau_{\text{eff,HeII}}$ that should be observed. Using 50 sightlines in the bootstrap calculation does not accurately represent the large intrinsic scatter seen in determining $\tau_{\text{eff,HeII}}$ from different sightlines at a given redshift. Furthermore, the variance estimated from 50 sightlines in a bootstrap realization does not reflect the state of observations entirely, since there is a relatively broad redshift distribution of the observed sightlines (see the observed points in [Figure 2](#)). Furthermore, the variance determined from using bootstrap resampling will only provide an estimate on the error in determining the mean, rather than capturing the intrinsic scatter of $\tau_{\text{eff,HeII}}$.

The shaded regions still provide valuable information about our ability to distinguish between various scenarios. In particular, note that at redshifts $z \gtrsim 3$, the shaded regions encompass many of the observed points (though, as mentioned above, the shaded error regions should extend to higher values of $\tau_{\text{eff,HeII}}$), as well as the values of $\tau_{\text{eff,HeII}}$ from distinct scenarios. Thus, the quantity $\tau_{\text{eff,HeII}}$ with only a handful of measurements is not a reliable method for determining the history of He II reionization.

3.2. Flux PDF

As discussed in [Paper II](#), another tool for analyzing the ionization state of the medium is the flux PDF. This

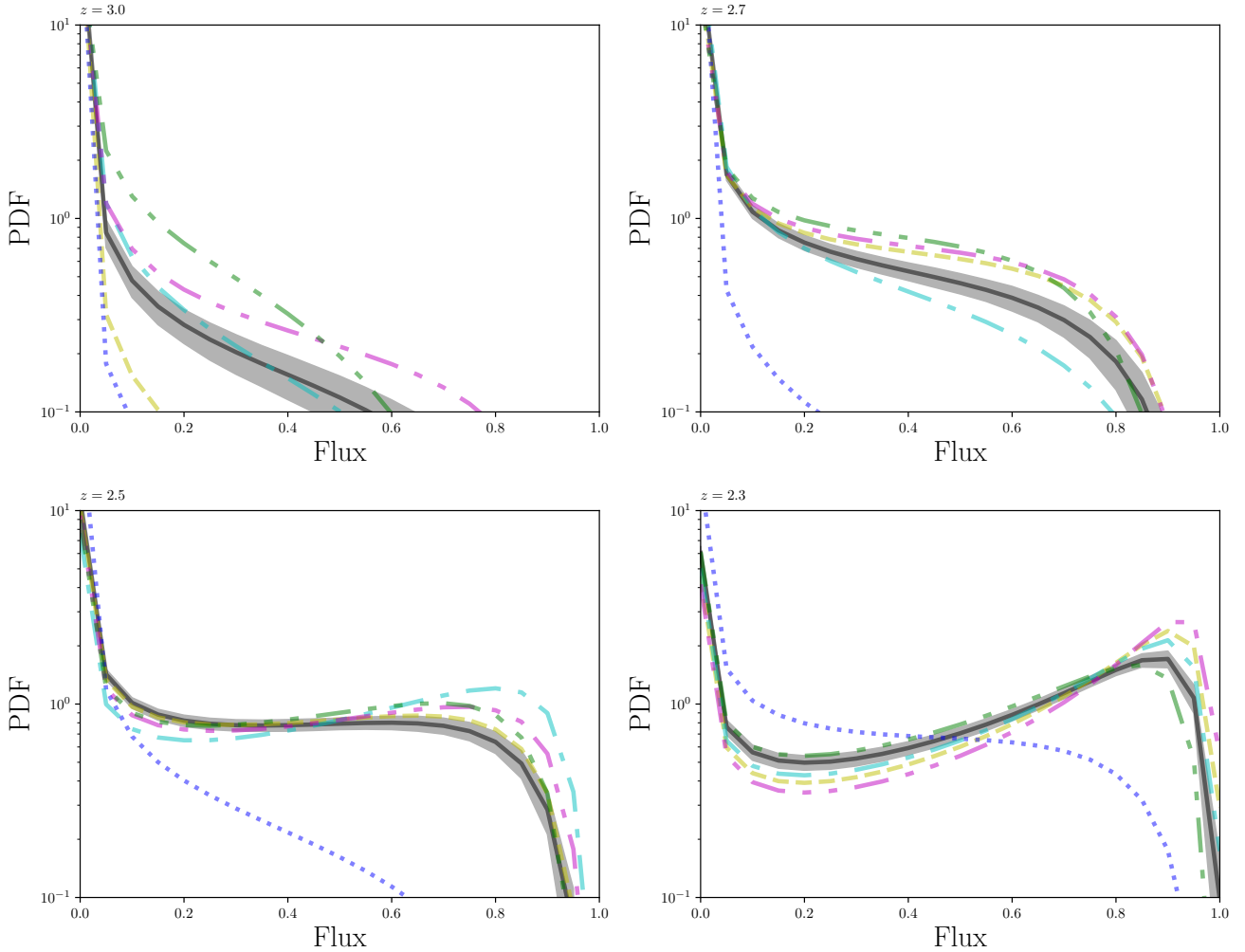


Figure 3. The flux PDF of the HeII Ly α forest at redshifts $z \sim 3$ (top left), $z \sim 2.7$ (top right), $z \sim 2.5$ (bottom left), and $z \sim 2.3$ (bottom right). The flux PDF is very sensitive to the tail end of reionization: most of the simulations have an ionization fraction $x_{\text{HeIII}} \gtrsim 0.99$ at $z \sim 2.7$, and yet have a comparatively low number of pixels with high transmission ($F \gtrsim 0.5$). Nevertheless, the ionization fraction can be determined from the overall shape of the PDF: the flux PDF of Simulation H3 at redshift $z \sim 2.3$ looks comparable to the other simulations at earlier times, such as at redshift $z \sim 2.7$. Accordingly, the flux PDF has a similar shape at comparable helium III ionization fractions, which will be discussed more in Figure 4. The shaded regions show the error in the determination of the mean of Simulation H1 computed using bootstrap resampling. For more details, see the discussion in Section 3.2.

measurement captures the distribution of flux for all pixels. As with $\tau_{\text{eff,HeII}}$, this statistic is most sensitive to the tail-end of reionization. Due to the low number of He II pixels with high transmission ($F \gtrsim 0.5$) before the end of reionization ($x_{\text{HeIII}} \gtrsim 0.99$), the flux PDF cannot provide detailed information while reionization is underway. However, it can still provide valuable information about the timing of reionization.

Figure 3 shows the He II flux PDF for the different simulations. The panels show the volume at redshifts $z \sim 2.7$ (top), $z \sim 2.5$ (bottom left), and $z \sim 2.3$ (bottom right). Note that at redshift $z \sim 2.7$, most of the simulations are 99% reionized. Despite this fact, there are comparatively few pixels with high transmission: for the fiducial case of Simulation H1, 90% of the pixels have

flux of $F \leq 0.5$. This relatively strong absorption is related to the strength of the Ly α transition, where only a small amount of He II is necessary to absorb most of the incoming radiation. Note, though, that measurement of the flux PDF can still be an important marker of the timing of reionization. As noted above, Simulation H3 reaches 99% reionization significantly later at $z_{99} \sim 2.23$, which is evident in the distinct shape of the flux PDF. In particular, there are far fewer pixels with $F \geq 0.5$ at all redshifts, indicative of its relatively late completion of reionization. The flux PDF of H3 at $z \sim 2.3$ is comparable to that of, *e.g.*, Simulation H1 at $z \sim 2.7$. Thus, by measuring the redshift when the central portion of the flux PDF is relatively flat (*e.g.*, when $\text{PDF}(F = 0.25) \approx \text{PDF}(F = 0.75)$), one can determine

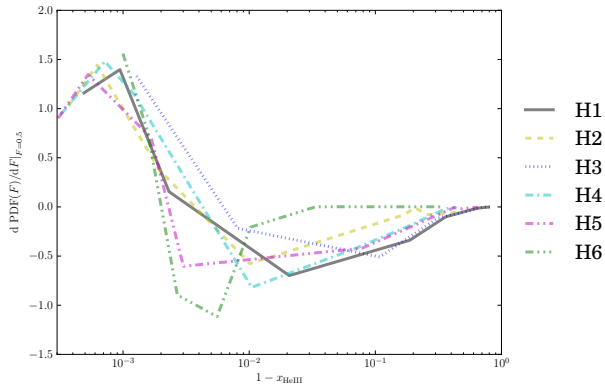


Figure 4. The derivative of the flux PDF at $F = 0.5$ as a function of the helium III fraction for the different simulations. The complement of the helium III fraction $1 - x_{\text{HeIII}}$ is shown, to emphasize the behavior at high ionization fractions. The helium fraction is shown instead of redshift to emphasize characteristics common to the different reionization scenarios. At early times (when $1 - x_{\text{HeIII}} \sim 1$), the slope of the flux PDF is typically flat or negative. The slope is negative for the majority of the ionization process, but becomes positive again following a 99% ionization fraction. This feature is common across quasar models, and thus represents a robust indicator of the timing for the end of helium reionization. Note that the simulations H3 and H6 do not reach ionization fractions greater than 99.9% ionized by $z \sim 2$.

the timing of when the volume is $\sim 99.9\%$ ionized. This point is addressed more directly in Figure 4 (discussed below).

The shaded error regions in Figure 3 show 1σ uncertainties, and are calculated using bootstrap resampling of 50 sightlines and computing the variance within each flux bin.² Moreover, the sightline length used is 10 proper Mpc, which is comparable to the distances reported in measurements (Worseck et al. 2014). In contrast to the shaded regions in Figure 2, these error regions are generally quite small, and do not significantly overlap with other simulations. This result demonstrates that only a few sightlines are necessary to determine the shape of the flux PDF. It should be noted that analogously to the H I flux PDF (and further discussed in Appendix B of Paper II), the continuum level of the measured spectra can have a dramatic effect on the shape of the flux PDF. Accordingly, uncertainty in this level can lead to systematic shifts in the calculated flux PDF. Nevertheless, Figure 3 shows that given low systematic uncertainties, the flux PDF of the He II Ly α forest can be a powerful tool for determining the ionization state of helium in the IGM.

Figure 4 shows the derivative of the flux PDF $d\text{PDF}(F)/dF$ at a value of $F = 0.5$ as a function of the

complement of He III ionization fraction $1 - x_{\text{HeIII}}$. This quantity is used instead of simply the ionization fraction to emphasize the behavior at high ionization levels. All of the reionization scenarios have been converted from redshift to ionization fraction in order to demonstrate uniformity across realizations. As discussed above, the transition from most pixels with values of $F \sim 0$ to $F \sim 1$ occurs relatively late in the ionization process. This transition can be captured in the change of the slope of the PDF at a value of $F = 0.5$: at early times and low ionization levels, the slope is negative with increasing flux values. Once the volume becomes $\sim 99\%$ ionized, the flux PDF flattens out. At even higher ionization levels, the slope becomes positive. As shown in Figure 4, the timing for these transitions is closely tied to the ionization fraction, rather than a specific redshift. Furthermore, as demonstrated with the relatively small statistical error bars in Figure 3, the flux PDF can be determined to high fidelity with relatively few He II sightlines. Assuming systematic uncertainties of observations can be sufficiently mitigated, this quantity represents a robust method for determining the endpoint of helium II reionization, to a much greater degree than the effective optical depth $\tau_{\text{eff,HeII}}$.

3.3. One-dimensional flux power spectra

In addition to the flux PDF, the one-dimensional power spectrum of the He II Ly α forest can be used to learn important information about the ionization state of the IGM. The overall amplitude of the power spectrum as well as the shape as a function of Fourier mode k will change as the ionization state and the size of ionized regions change. As with the one-dimensional power spectrum for H I, the amplitude on large scales is related to the optical depth $\tau_{\text{eff,HeII}}$, with higher amplitudes corresponding to higher values of $\tau_{\text{eff,HeII}}$ (see Figure 2).

Figure 5 shows the one-dimensional power spectrum of the He II Ly α forest. The primary difference between the simulations is in the amplitude of the power spectra. At a given redshift, the amplitude of the power spectrum is directly related to the value of τ_{eff} . Note that Simulation H3 has the largest value of τ_{eff} at a given redshift (as shown in Figure 2), and also has the largest amplitude in Figure 5. This can be understood in terms of the amplitude of fluctuations in the flux field: when the IGM has a relatively low value of τ_{eff} , then all points in the volume have a similarly (high) value of flux. These differences in flux are driven primarily by correlations with the radiation field. Not only is the fraction of He III higher in regions of high radiation intensity, but the temperature is also greater. Both of these effects contribute to a lower value of $\tau_{\text{eff,HeII}}$, or a higher value of flux F . The combination leads to highly correlated regions of high flux and low flux, increasing the ampli-

² Note though that, as mentioned in Section 3.1, using 50 samples in the bootstrap realization for determining the variance may be overly optimistic.

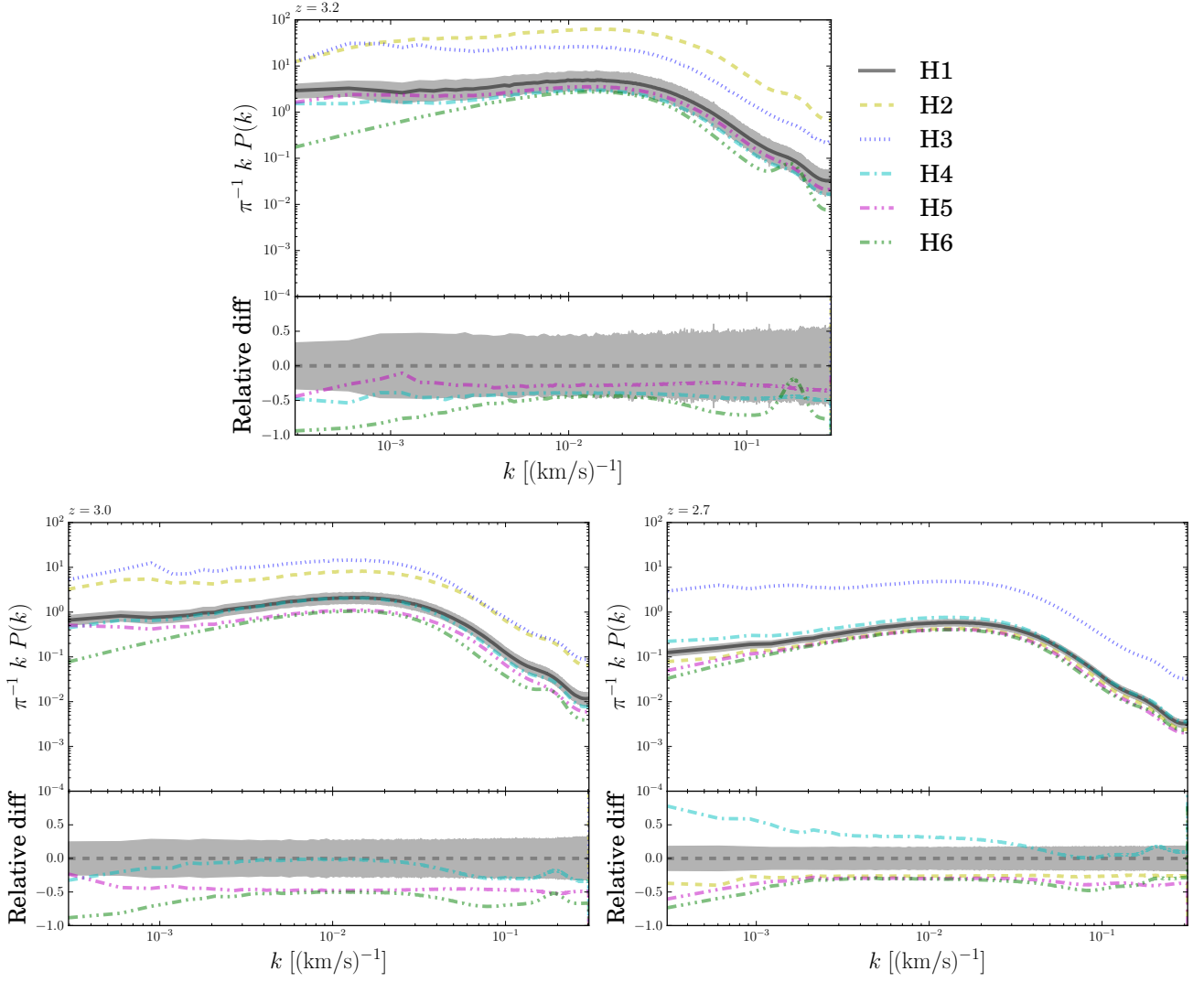


Figure 5. One-dimensional flux power spectra of the He II Ly α forest, at redshift $z \sim 3.2$ (top), $z \sim 3$ (bottom left), and $z \sim 2.7$ (bottom right). These redshifts are different than the ones in Figure 3 because the change in amplitude of the power spectra are more evident earlier in the reionization process. At a given redshift, there is a marked difference in the overall amplitudes of the power spectrum. These changes are correlated with the value of τ_{HeII} at a given redshift. Compare to Figure 2, and note that the amplitude of the power spectrum largely tracks the values of τ_{eff} . See the text for additional discussion.

tude of the power spectrum. At the same time, it is not solely the radiation field that controls the amplitude of the power spectrum, as Simulation H6 has a uniform radiation field. In this simulation, the differences are driven primarily by the local gas density, and so there is no corresponding correlation between regions of high and low flux.

At $z \sim 2.7$, the difference in the power spectrum amplitude of Simulation H3 at all scales is an order of magnitude larger than that of the other simulations. Such a dramatic difference should be detectable, and would allow for a straightforward determination of the helium ionization state of the IGM. Most importantly, the amplitude of the flux power spectrum as a function of redshift are clear and pronounced, even for reionization histories that are not fully reionized. Hence, the

one-dimensional power spectrum can be a window into helium II reionization at times prior to 99% ionization.

The shaded regions show 1σ uncertainty in the measurements using 50 sightlines and bootstrap resampling, with the same rationale as that discussed regarding Figure 3 in Section 3.2. Unlike the approach taken there, though, the entire sightline is used rather than a 10 Mpc segment. By using the entire sightline, there are no issues related to broken periodicity when performing the Fourier transform for the power spectrum calculation.³

³ Note though that at $z \sim 3$, the sightlines from the simulation are ~ 71 proper Mpc, which is almost an order of magnitude larger than the observational sightlines (which as stated above are ~ 10 proper Mpc). There is thus implicitly additional information in each of the simulated sightlines compared to the observational

At the earliest redshift ($z \sim 3.2$), there is a relatively large uncertainty, so that at most scales, several of the reionization histories are expected to lie within 1σ of each other. However, simulations with vastly different values of τ_{eff} (as in Simulations H2 and H3 in Figure 2) still show a distinct change in amplitude of the power spectrum. Thus, the one-dimensional power spectrum can serve as another measurement of the overall opacity of the volume.

At lower redshift, the uncertainty of the power spectra decreases noticeably. As a result, in principle it becomes easier to distinguish the histories. At the same time, there is significant overlap in several of the histories, which is due to having comparable value of τ_{eff} . Some of the largest differences that remain are at large scales. As with the H I Ly α forest (and discussed in Paper II), these differences might be attributable to the large-scale radiation field. Because the radiation field is highly non-uniform He II-ionizing radiation originating from quasars (as opposed to the H I forest that has a largely uniform background component from galactic radiation), the large-scale power may reflect the degree of bias in the sources. Note in particular that Simulation H6, which has only a uniform UV background and no explicit sources, has consistently the lowest large-scale power, despite having one of the earliest reionization times. At all redshifts considered, this simulation shows a lack of power compared to the simulations with explicit sources. Thus, the large-scale power may be a way to learn about the bias of sources of helium II reionization.

Nevertheless, there are potential observational complications associated with determining the one-dimensional flux power spectrum. Due to the overall low value of flux in the He II Ly α forest before the conclusion of reionization, it is difficult to determine the continuum level, and hence the flux measurement. Determining the global (low) flux value can lead to an incorrect normalization, and hence raise or lower the large-scale power spectrum amplitude. Despite this difficulty, the one-dimensional power spectrum remains one of the few probes that can detect the ionization level of helium before completion, and does not rely on calibrating other measurements of the IGM.

4. DISCUSSION

One very pertinent question with these measurements is the degree to which the reionization history can be determined with a limited number of observations. As dis-

cussed in Section 1, to date there have been only about 50 observations of the He II Ly α forest (Syphers et al. 2012). We have shown in Secs. 3.2 and 3.3 that the flux PDF and one-dimensional power spectrum provide significant information about the ionization state of helium. However, it is reasonable to wonder to what extent current observations are able to determine the ionization state of the IGM.

To this end, we have used bootstrap resampling using 50 sightlines to estimate the standard deviation for our different scenarios. Figures 3 and 5 show the 1σ dispersion as measured for 50 sightlines. As noted in the earlier discussion, the ionization state of helium may be readily detectable in the flux PDF measurement. Even accounting for uncertainty in the continuum level of the forest, the shape of the flux PDF varies strongly as a function of ionization fraction. This variation in shape is significantly larger than the inherent variation of the flux PDF, and so even with comparatively few sightlines, a meaningful determination of the ionization level of helium maybe possible given the current data. Figure 4 shows that the slope of the flux PDF is capable of well-characterizing the timing of the end of reionization, since the slope is highly correlated with the ionization fraction rather than a particular redshift. Accordingly, the flux PDF should be a powerful tool for learning more about helium II reionization.

Furthermore, the He II one-dimensional power spectrum on large scales could help determine the bias of sources driving helium II reionization. Note that there is more than an order of magnitude difference in the amplitudes at large scales (*e.g.*, $k = 3 \times 10^{-3} \text{ (km/s)}^{-1}$), which should be detectable. In addition to the overall amplitude, the shape of the power spectrum on large scales is greatly influenced by the relative bias of the sources: note that all simulations with explicit sources (H1-H5) have a relatively flat power spectrum at large scales, but the uniform UV background featured in Simulation H6 shows decreasing amplitude with decreasing k . This is likely related to the radiation field properties: the differences in the helium II ionization fraction in Simulation H6 are driven primarily by gas density fluctuations, since the same ionization field is seen at all points in the volume. Accordingly, there is less correlation between regions of high flux and low flux in terms of helium ionization level as well as temperature, and thus less power. At the same time, determining the continuum level in observations is difficult for such small flux levels, and errors in its determination may power spectrum amplitude.

5. CONCLUSION

To date, the He II Ly α forest has largely only been used to determine the value of $\tau_{\text{eff,HeII}}$. As can be seen

ones, though there are fewer numerical artifacts introduced by using the whole sightline and not explicitly breaking periodicity in the Fourier transform.

from Figure 2, there is a very large dispersion in this measurement, owing to the large sightline-to-sightline variations. Thus, determining the reionization history from this quantity alone is very difficult, and leads to large uncertainties in the determination of the redshift of reionization. Additionally, as discussed in Section 3.1, this measurement is largely sensitive to the tail-end of reionization, and does not yield much information about the intermediate stages of the reionization process. Accordingly, new applications of the He II Ly α forest would be beneficial for learning more about the timing and duration of reionization.

To this end, we have presented the flux PDF and the one-dimensional power spectrum as ways to break the degeneracy present in τ_{eff} . These differences are generally quite large between different simulations, in some cases being larger than an order of magnitude. Further surveys will hopefully be able to take advantage of these pronounced differences, and begin to measure the timing and duration of helium II reionization.

This work was supported in part by NASA grants NNX14AB57G and NNX12AF91G and NSF grant AST15-15389.

REFERENCES

- Battaglia, N., Trac, H., Cen, R., & Loeb, A. 2013, *ApJ*, 776, 81
 Becker, G. D., Bolton, J. S., Haehnelt, M. G., & Sargent, W. L. W. 2011, *MNRAS*, 410, 1096
 Becker, G. D., Hewett, P. C., Worseck, G., & Prochaska, J. X. 2013, *MNRAS*, 430, 2067
 Boera, E., Murphy, M. T., Becker, G. D., & Bolton, J. S. 2014, *MNRAS*, 441, 1916
 Bolton, J. S., Oh, S. P., & Furlanetto, S. R. 2009, *MNRAS*, 395, 736
 Bolton, J. S., Puchwein, E., Sijacki, D., et al. 2016, *ArXiv e-prints*, arXiv:1605.03462
 Compostella, M., Cantalupo, S., & Porciani, C. 2013, *MNRAS*, 435, 3169
 —. 2014, *MNRAS*, 445, 4186
 Croft, R. A. C., Weinberg, D. H., Katz, N., & Hernquist, L. 1997, *ApJ*, 488, 532
 Dawson, K. S., Schlegel, D. J., Ahn, C. P., et al. 2013, *AJ*, 145, 10
 Dixon, K. L., & Furlanetto, S. R. 2009, *ApJ*, 706, 970
 Dixon, K. L., Furlanetto, S. R., & Mesinger, A. 2014, *MNRAS*, 440, 987
 Furlanetto, S. R., & Oh, S. P. 2008a, *ApJ*, 682, 14
 —. 2008b, *ApJ*, 681, 1
 —. 2009, *ApJ*, 701, 94
 Gleser, L., Nusser, A., Benson, A. J., Ohno, H., & Sugiyama, N. 2005, *MNRAS*, 361, 1399
 Gunn, J. E., & Peterson, B. A. 1965, *ApJ*, 142, 1633
 Haardt, F., & Madau, P. 2012, *ApJ*, 746, 125
 Hinshaw, G., Larson, D., Komatsu, E., et al. 2013, *ApJS*, 208, 19
 Iršič, V., Viel, M., Haehnelt, M. G., et al. 2017, *Physical Review D*, 96, 023522
 Jakobsen, P., Boksenberg, A., Deharveng, J. M., et al. 1994, *Nature*, 370, 35
 La Plante, P., & Trac, H. 2016, *ApJ*, 828, 90
 La Plante, P., Trac, H., Croft, R., & Cen, R. 2017, *ApJ*, 841, 87
 Lee, K.-G., Hennawi, J. F., Spergel, D. N., et al. 2015, *ApJ*, 799, 196
 Lusso, E., Worseck, G., Hennawi, J. F., et al. 2015, *MNRAS*, 449, 4204
 Masters, D., Capak, P., Salvato, M., et al. 2012, *ApJ*, 755, 169
 McDonald, P., Miralda-Escudé, J., Rauch, M., et al. 2001, *ApJ*, 562, 52
 McGreer, I. D., Jiang, L., Fan, X., et al. 2013, *ApJ*, 768, 105
 McQuinn, M., Hernquist, L., Lidz, A., & Zaldarriaga, M. 2011, *MNRAS*, 415, 977
 McQuinn, M., Lidz, A., Zaldarriaga, M., et al. 2009, *ApJ*, 694, 842
 Møller, P., & Jakobsen, P. 1990, *A&A*, 228, 299
 Puchwein, E., Bolton, J. S., Haehnelt, M. G., et al. 2015, *Monthly Notices of the Royal Astronomical Society*, 450, 4081
 Reimers, D., Kohler, S., Wisotzki, L., et al. 1997, *A&A*, 327, 890
 Ross, N. P., McGreer, I. D., White, M., et al. 2013, *ApJ*, 773, 14
 Schaye, J., Theuns, T., Leonard, A., & Efstathiou, G. 1999, *MNRAS*, 310, 57
 Syphers, D., Anderson, S. F., Zheng, W., et al. 2009a, *ApJS*, 185, 20
 —. 2012, *AJ*, 143, 100
 Syphers, D., & Shull, J. M. 2014, *ApJ*, 784, 42
 Syphers, D., Anderson, S. F., Zheng, W., et al. 2009b, *ApJ*, 690, 1181
 Trac, H., & Cen, R. 2007, *ApJ*, 671, 1
 Trac, H., Cen, R., & Loeb, A. 2008, *ApJL*, 689, L81
 Trac, H., & Pen, U.-L. 2004, *NewA*, 9, 443
 Viel, M., Lesgourgues, J., Haehnelt, M. G., Matarrese, S., & Riotto, A. 2005, *PhRvD*, 71, 063534
 White, M., Myers, A. D., Ross, N. P., et al. 2012, *MNRAS*, 424, 933
 Worseck, G., Prochaska, J. X., Hennawi, J. F., & McQuinn, M. 2014, *ArXiv e-prints*, arXiv:1405.7405
 Worseck, G., Prochaska, J. X., McQuinn, M., et al. 2011, *ApJL*, 733, L24
 Zheng, W., Anderson, S. F., Kriss, G. A., et al. 2005, in *IAU Colloq. 199: Probing Galaxies through Quasar Absorption Lines*, ed. P. Williams, C.-G. Shu, & B. Menard, 484–486
 Zheng, W., Meiksin, A., Pifko, K., et al. 2008, *ApJ*, 686, 195